High-Pressure Melting Curve of FeH: Implications for Eutectic Melting between Fe and Non-Magnetic FeH

Shoh Tagawa[1,2], George Helffrich[1], Kei Hirose[1,2], and Yasuo Ohishi[3]

[1]Earth-Life Science Institute, Tokyo Institute of Technology, Tokyo, Japan
[2]Department of Earth and Planetary Science, The University of Tokyo, Tokyo, Japan
[3]Japan Synchrotron Radiation Research Institute, SPring-8, Hyogo, Japan

Correspondence to: K. Hirose (kei@elsi.jp)

Key Points:

- We determined the melting curve of non-magnetic FeH to 152 GPa based on synchrotron XRD measurements.
- XRD data indicated congruent melting of non-magnetic FeH, suggesting eutectic melting between Fe and FeH above ~40 GPa.
- Similar dT/dP slopes between the melting curves of Fe and FeH imply little pressure dependence of the Fe-FeH eutectic liquid composition.

Abstract While hydrogen could be an important light alloying element in planetary iron cores, phase relations in the Fe-FeH system remain largely unknown at high pressures and temperatures (P-T). A speculative Fe-H_2 phase diagram has been proposed assuming continuous solid solution between Fe and FeH and eutectic melting between FeH and H_2. Recent studies revealed that stoichiometric FeH becomes non-magnetic above ~40 GPa, which might affect its melting behavior. Here we examined the melting curve of non-magnetic FeH between 43 and 152 GPa by a combination of laser-heated diamond-anvil cell (DAC) techniques and synchrotron X-ray diffraction (XRD) analyses. The melting temperature was determined by employing the appearance of additional hazy XRD signals upon quenching temperature as a melting criterion. We also performed thermodynamic modeling, which well reproduces the change in the curvature of FeH melting curve upon the loss of magnetism and extrapolates the experimental constraints to inner core pressures. The XRD data showed that non-magnetic FeH melts congruently at temperatures higher than the known eutectic melting curve for FeH_x ($x > 1$). Combined with the fact that the endmembers exhibit different crystal structures, these results indicate that Fe and non-magnetic FeH form a eutectic system. The dT/dP slope of the

FeH melting curve is comparable to that for Fe, suggesting that the eutectic liquid composition of $FeH_{0.42}$ (Fe + 0.75 wt% H) previously estimated at ~40 GPa changes little with increasing pressure.

Plain Language Summary It is likely that a large amount of water was transported to the Earth during its accretion and hydrogen was incorporated into core-forming metals. Indeed, recent calculations found that hydrogen could be an important light element in both the outer and inner core to explain the observed density and velocities. Nevertheless, experimental study of Fe-H alloys has been challenging, in part because hydrogen is almost insoluble in iron at 1 bar. Here we determined the melting curve of stoichiometric FeH in the non-magnetic state from 43 to 152 GPa based on XRD measurements. The melting temperature of FeH increases rapidly with compression upon the loss of local spin moment. The XRD spectra show that stoichiometric FeH melts congruently, suggesting eutectic melting between Fe and FeH that is supported by the different crystal structures between these two endmembers. Since the dT/dP slopes of the Fe and FeH melting curves are similar, it is likely that the Fe-FeH eutectic liquid composition is little dependent on pressure and could be around $FeH_{0.42}$ at inner core conditions, which gives the upper bound for the hydrogen concentration in the outer core.

1. Introduction

Hydrogen (H) is likely to be an important light element in the cores of terrestrial planets (Hirose et al., 2021; Yoshizaki & McDonough, 2020). According to planet formation theories (Raymond et al., 2007; Walsh et al., 2011; Sato et al., 2016), water may have been delivered to the growing Earth and Mars in large quantities. The high metal/silicate partition coefficient of H found in recent experimental and computational works suggest that most of the water transported to our planet was sequestered mainly as up to ~1 wt% H in the core (Tagawa et al., 2021; Li et al., 2020; Yuan & Steinle-Neumann, 2020). Indeed, H-bearing iron (Fe) alloys can explain the observed density and seismic-wave velocities in both the liquid outer core (Umemoto & Hirose, 2015, 2020) and the solid inner core (Wang et al., 2021; He et al., 2022). In addition, the recent marsquake observations by the InSight probe revealed that the Martian core is less dense than previously thought, possibly including 1–2 wt% H in addition to sulfur (S) (Stähler et al., 2021).

The Fe-FeH phase diagram is of great importance to understand the present state and composition of planetary metallic cores. However, it is still vaguely known. Fe-H alloys

must be examined under high pressure, because the solubility of H in Fe is negligibly small at 1 bar and rapidly increases with increasing pressure (e.g., Fukai & Suzuki, 1986). Fukai (1992) speculated on the melting and subsolidus phase relations in the Fe-H_2 system at >100 GPa, assuming that Fe and FeH form a continuous solid solution (Figure 1a). While earlier experiments on the Fe-H(±Ni) system supported Fukai's phase diagram below ~20 GPa (Sakamaki et al., 2009; Shibazaki et al., 2014), it has not been verified at higher pressures. Experiments on FeH should be performed under H-undersaturated conditions otherwise FeH_2 and FeH_3 form above 60 GPa (Pépin et al., 2014).

The crystal structure and melting temperature of stoichiometric FeH is a key to the Fe-FeH phase diagram. Previous studies have shown that it adopts the face-centered cubic (fcc) structure above ~50 GPa and ~1000 K (Kato et al., 2020; Tagawa et al., 2022), which is different from the hexagonal close-packed (hcp) structure for Fe at core conditions (Komabayashi et al., 2009). Tagawa et al. (2022) also demonstrated that FeH loses its local spin moment above ~40 GPa. The melting curve of non-magnetic fcc FeH is not known. If Fe and FeH form a continuous solid solution as supposed by Fukai (1992), the solidus temperature of FeH corresponds to the eutectic temperature in the FeH-H_2 system (Sakamaki et al., 2009; Shibazaki et al., 2014; Hirose et al., 2019) (Figure 1a). However, the different crystal structure between Fe and FeH above ~50 GPa will probably change the Fe-FeH phase diagram significantly.

In this study, we examined the melting curve of fcc stoichiometric FeH in a pressure range between 43 and 152 GPa in a laser-heated DAC, based on synchrotron XRD measurements *in-situ* at high *P*-*T*. The results demonstrate that the d*T*/d*P* slope of the melting curve of non-magnetic FeH is substantially larger than that observed for the magnetic phase below 20 GPa (Sakamaki et al., 2009). In addition, XRD spectra indicated that melting of FeH is congruent. It indicates that non-magnetic FeH melts at a temperature maximum and forms a eutectic system with Fe, which is supported by the different crystal structures between these two endmembers. The high d*T*/d*P* slope of the FeH melting curve is similar to that of Fe, suggesting that the Fe-FeH eutectic liquid composition that places the upper bound for H concentration in the Earth's liquid outer core is little dependent on pressure.

2. Experimental Methods

2.1. High-pressure Experiments

High *P*-*T* conditions were generated by using laser-heated DAC techniques up to 152 GPa and 4630 K (Figure 2). We employed diamond anvils with beveled 300, 200, and

120 μm culet size. Sample configuration was similar to that reported in Tagawa et al. (2016). Inside the preindented 20–25 μm thick rhenium (Re) gasket, the NaCl inner gasket prepared with a Focused Ion Beam (FIB) was employed to prevent H loss to the Re gasket. The surface of the diamond anvils was coated with titanium such that we could avoid the failure of diamond anvils (Ohta et al., 2015). We loaded a ~10 μm thick pure Fe foil (>99.999% purity, Toho Zinc) between the NaCl plates, which served not only as a pressure medium but also as a pressure marker and a hydrogen insulator. After drying a whole DAC in an oven, we cryogenically loaded liquid H_2 at temperatures below 20 K (Chi et al., 2011; Tagawa et al., 2016). The sample was then weakly compressed and brought back to room temperature. After it was further compressed to 15–30 GPa, double hcp (dhcp) (± fcc) stoichiometric FeH was synthesized by laser heating Fe + H_2 to ~1000 K under hydrogen-saturated conditions (Hirao et al., 2004; Tagawa et al., 2016; Kato et al., 2020) (dhcp FeH was sometimes obtained without heating). Subsequently pressure was fully released under liquid nitrogen temperature (~85 K) in an N_2 atmosphere, and we opened the sample chamber to remove excess H_2 without decomposition of FeH (note that FeH is metastably quenchable to 1 bar below ~200 K as demonstrated by Antonov et al., 2019). The sample was repressurized to >5 GPa under cryogenic temperature and further to a pressure of interest at 300 K.

Heating was made along with *in-situ* high *P-T* XRD measurements at the beamline BL10XU, SPring-8 synchrotron facility (Hirao et al., 2020). The sample was heated from both sides using a couple of 100 W single-mode Yb fiber lasers. A laser beam was converted to one with a flat energy distribution by beam-shaping optics, and the laser-heated spot was 30–40 μm across. Temperature was measured by a spectro-radiometric method. The mean sample temperature, T_{mean}, is the average over 6 μm area at a laser-heated hot spot, which corresponds to the X-ray beam size, for both sides. In addition, Table 1 also gives the highest temperature at the center of the hot spot, T_{max}, that is more relevant to melting. The uncertainties in T_{mean} and T_{max} may be ±5% according to Mori et al. (2017). A monochromatized incident X-ray beam with an energy of ~30 keV was focused to 6 μm in diameter on a sample. Diffraction patterns were collected on a flat panel detector (PerkinElmer) with exposure time of 1 sec at 300 K before and after heating and at high temperatures. The XRD patterns also provided the unit-cell volume of B2-type NaCl, from which pressure was determined at both 300 K and high temperatures (Dorogokupets & Dewaele, 2007) considering its effective temperature (Campbell et al., 2009); $T_{NaCl} = \frac{3\times T_{mean}+300}{4} \pm \frac{T_{mean}-300}{4}$. This method for determining pressure at high temperature based on the volume of the pressure medium has been validated in Tagawa

et al. (2022) by simultaneously using NaCl and KCl; since the thermal expansivity of NaCl is much larger than that of KCl, the effect of temperature variation is larger, but NaCl gave pressures at high temperatures very similar to those by KCl.

After melting experiments, the sample was recovered from the DAC in run #1. We prepared its cross section at the center of a laser-heated spot parallel to the compression axis by using a focused Ga ion beam, FIB (FEI, Versa 3D DualBeam). The melting texture was examined by a field-emission-type scanning electron microscope (SEM).

2.2. Thermodynamic Modeling

Our thermodynamic model is based on low-pressure metallurgical models for Fe-Sm hydride and Fe-Ti hydride alloys (Zinkevich et al., 2002; Kivilahti & Miettinen, 1987) that we extended to high pressures. Solid iron hydrides FeH_x are not stoichiometric, exhibiting H contents x in the range $0 \leq x \leq 1$ and possibly $x > 1$ (Fukai, 1992; Sugimoto & Fukai, 1992; Hirose et al., 2019; Ikuta et al., 2019).

We model the melting experiments by calculating the P and T trajectory of the liquid-solid boundary at constant composition. Here, the free energy $G(P,T)$ of the solid fcc FeH (s) and liquid FeH (l) are equal, or

$$\Delta G = G^l - G^s = 0. \quad (1)$$

Following Helffrich & Connolly (2009), G's P and T dependence is separated into a room pressure (1 bar) T dependence given by polynomial expressions in T (Zinkevich et al., 2002) and a Birch-Murnaghan dependence on P which is third-order in finite strain $f = (1/2)[(V_0/V)^{2/3} - 1]$. Fcc FeH also requires the magnetic contribution to free energy, G_{mag}. For a phase ϕ,

$$G^{\phi}(P,T) = G^{\phi}(T) + \int_0^P V_x^{\phi}(T,p)\, dp + G_{\mathrm{mag}}^{\phi} \quad (2)$$

V^{ϕ}_x is a composition-dependent volume that depends on x, the stoichiometric coefficient in FeH_x, defined as

$$V_x^{\phi} = V_{\mathrm{FeH}_x}^{\phi}(x) = V_{\mathrm{Fe}}^{\phi} + xV_{\mathrm{H}}^{\phi}. \quad (3)$$

A polynomial representation for the thermal expansivity, $\alpha(T)$, provides the temperature part of the volume dependence (see Table 2), which is itself composition dependent. The pressure contribution to the free energy in equation (2) is evaluated through a compositionally-dependent bulk modulus K_x and its pressure derivative K_x' (Table 2). The assumption that $K' = \delta_T$ provides K's temperature dependence (Helffrich & Connolly,

2009),

$$K_x(T) = K_{x,0} exp\left[-\delta_T \int_{T_0}^{T} \alpha_x(t)\, dt\right] \quad (4)$$

The Birch-Murnaghan relation's P dependence is implicit in

$$P = 3K_x(T) f (1 + 2f)^{5/2}(1 + 2\psi f), \quad (5)$$

with $\psi = 3(K_x' - 4)/4$. The pressure contribution to G is obtained by finding f for a given P and then integrating (5) by parts,

$$\int V dP = [PV]_{0,T}^{P,T} - \int P dV = [PV]_{0,T}^{P,T} - \int P \frac{dV}{df} df. \quad (6)$$

The magnetic contribution to the free energy depends on the compositionally dependent Curie/Néel temperature $T_{C,x}$ and magnetic moment β_x, and a magnetic enthalpy parameter p that only depends on structure

$$G_{\mathrm{mag}(x)} = RT \log(\beta_x + 1) \times g\left(T/T_{C,x}, p\right) \quad (7)$$

whose rationale and expression for g may be found in Hillert & Jarl (1978).

The polynomials for the 1 bar G temperature dependence are from Zinkevich et al. (2002). To refine the physical properties of pure iron, we use those data and modify the volume integral contributions to fit a suite of experimental constraints. For iron, we use Komabayashi & Fei's (2010) experimental data points for the bcc-fcc boundary, the body-centered cubic (bcc)-hcp boundary, and the fcc-hcp boundary, and the fcc-hcp boundary from Komabayashi (2014), and the experimental melting points below the liquid-fcc-hcp triple point from Anzellini et al. (2013). We use a nonlinear minimization scheme (R Core Team, 2018) for the liquid parameters V_0, α, K, and K' that yield $\Delta G = 0$ at the experimentally determined P and T conditions, plus auxiliary constraints that prevent bcc and fcc iron from becoming stable at inner core conditions.

$G(T)$ for compounds like FeH_x are built from element contributions and additional terms (Zinkevich et al. 2002). Since we are only interested in the FeH composition, we can simplify these terms to the endmember stoichiometric component FeH and dispense with the complexity of nonideal mixing.

Hydrogen solubility in liquid Fe is more complex. Previous eutectic melting experiments in Fe-H (Hirose et al., 2019) suggested that melts yielded FeH_x liquid compositions with $0 \leq x \leq 2$. Our experiments (Table 1) provide iso-composition melting points of fcc FeH, so we specialize the liquid properties to that of $x = 1$. Along with Sakamaki et al.'s (2009) data for fcc FeH_x (with $x \approx 1$), these provide a way to estimate the required thermophysical

properties of FeH_x ($x \leq 1$) liquids — V_0, α, K, and K' — and for solid fcc FeH — β_x and $T_{C,x}$. The values are listed in Table 2.

3. Results

Melting was detected at six *P-T* conditions from 43 and 152 GPa in five separate runs (Table 1). In each experiment, the dhcp FeH sample underwent a full transformation to the fcc structure when it was first heated to >1500 K, consistent with previous theoretical and experimental studies (Isaev et al., 2007; Thompson et al., 2018; Kato et al., 2020). Neither FeH_2 nor FeH_3 was formed upon heating above 60 GPa (Pépin et al., 2014), which proved no excess hydrogen remained in the sample chamber. As demonstrated by earlier total energy calculations (Tagawa et al., 2022), fcc stoichiometric FeH is non-magnetic in this pressure range while it is magnetic at lower pressures. The previous experiments by Tagawa et al. (2022) showed that fcc FeH becomes less compressible above 41 GPa at room temperature, supporting the magnetic transition to non-magnetic. We confirmed each time at 300 K before and after melting the sample that the unit-cell volumes of the sample, including those of crystals that formed upon quenching temperature, were consistent with the compression curve of stoichiometric FeH (Tagawa et al., 2022).

In the first three runs, we determined the melting temperature of stoichiometric FeH while collecting the *P-V-T* data for the fcc phase. Such *P-V-T* data obtained in these three experiments and the high-temperature equation of state of fcc non-magnetic FeH have been reported in Tagawa et al. (2022) (the same run numbers were used). The *P-T* conditions at which the volume data were collected for the solid sample are plotted in Figure 2 (see small blue circles).

In run #1, we started heating at 62 GPa and 1800 K and observed a complete transformation from dhcp to fcc FeH (Figure 3a). We increased temperature stepwise to T_{max} = 2480 K and then rapidly quenched to 300 K by shutting down the laser beam. The unit-cell volume of the sample found at room temperature was on the compression curve of non-magnetic fcc FeH (Tagawa et al., 2022). Subsequently this sample was heated to higher temperature, T_{max} = 2740 K. Upon quenching temperature, additional "hazy" diffraction signals appeared close to the fcc peaks in the 2D and 1D XRD spectra (Figures 3c, d), which was not observed when quenching the sample from T_{max} = 2480 K (Figure 3b). This additional signal may have originated from incomplete fcc-like crystals with irregular planar stacking that were formed from liquid upon rapid temperature quenching. We recovered this sample and examined its texture on its cross section at the center of a laser-heated spot. The NaCl grains were found within FeH metal, which clearly indicates

that the sample was molten (Figure 4). These observations indicate that the sample did not melt to 2480 K but melted at 2740 K at 67–69 GPa (Figure 2). We also noted that FeH melted congruently (liquid FeH coexisted with solid FeH) since no Fe-H alloys other than stoichiometric FeH formed from liquid upon quenching temperature; liquid Fe-H crystallized Fe-H with almost equivalent H concentration at quenching (Hirose et al., 2019; Tagawa et al., 2021).

Similarly in runs #2–#5, we explored the melting of stoichiometric FeH, by employing the appearance of the additional hazy diffraction signal observed upon quenching temperature as a melting criterion. In run #2, the sample was compressed to 138 GPa and then heated. The hazy XRD signal was not observed when the sample temperature was quenched from T_{max} = 3900 K at 149 GPa. It was detected in the next heating cycle when the sample was quenched from T_{max} = 4630 K at 152 GPa, the highest *P*-*T* condition in the present study (Figure 2). In run #3, we collected the volume data for solid fcc FeH in a wide *P*-*T* range from 40 GPa/1600 K to 136 GPa/3600 K, repeating a number of heating cycles (Tagawa et al., 2022). Melting of the sample was not observed when quenched from 3560 K/113 GPa and 3610 K/135 GPa. On the other hand, the hazy signal from quenched liquid was obtained when the sample was heated to 3860 K/121 GPa and 4210 K/142 GPa. Note that since FeH melted congruently, melting did not cause heterogeneity in hydrogen concentration in the sample. Indeed, we observed only peaks from stoichiometric FeH along with the hazy signal and those from the NaCl pressure medium; the unit-cell volumes of FeH collected at room temperature were always plotted in a single *P*-*V* curve (Tagawa et al., 2022).

Runs #4 and #5 were carried out at 40–50 GPa, in order to determine the melting temperature near conditions where stoichiometric FeH loses its local spin moment (Tagawa et al., 2022). In run #4, we observed no signs of melting when quenching from T_{max} = 1830 K at 43 GPa but clearly obtained the additional hazy XRD signal after heating to T_{max} = 2110 K at 45 GPa (Figure 2). We rapidly quenched the sample only when heating to T_{max} = 2170 K at 47 GPa in run #5.

The melting curve of FeH was obtained by fitting the thermodynamic model to these not-melting and melting data along with those previously reported below 20 GPa (Sakamaki et al., 2009). Its d*T*/d*P* slope becomes substantially larger due to the loss of magnetism above ~40 GPa (Tagawa et al., 2022). The melting point of non-magnetic FeH is higher than the eutectic melting temperature of FeH_x ($1 < x < 2$) observed between 43 and 127 GPa (Hirose et al., 2019) (Figure 2). Note that the melting temperature of magnetic FeH found below 20 GPa corresponds to the eutectic temperature between FeH and H_2 (Fukai,

1992) (Figure 1a).

We do not model a change in volume at the magnetic to non-magnetic transition because it was not clearly observed in the compression curve of FeH reported by Tagawa et al. (2022). Omitting this detail simplifies the model at the cost of poorer constraints on fcc FeH's magnetic properties and the liquid bulk modulus: μ_B and K trade off since the melting curve slope is $dP/dT = \Delta S/\Delta V$ and μ_B affects ΔS.

4. Discussion

The present experiments suggest that the loss of local spin moment stabilizes solid fcc FeH to higher temperatures. FeH is not stable at ambient pressure because of the negligible solubility of hydrogen in iron (e.g., Fukai & Suzuki, 1986). Above ~5 GPa where FeH is stabilized (Sakamaki et al., 2009), Fe and FeH probably form a continuous solid solution in the fcc structure (Fukai, 1992; Shibazaki et al., 2014) (Figure 1a). At pressures greater than ~15 GPa, hcp Fe appears instead of the bcc phase at relatively low temperatures, which complicates the Fe-FeH phase diagram (Figure 1b). Stoichiometric FeH becomes non-magnetic at 41 GPa at 300 K (Tagawa et al., 2022). The melting temperature of the non-magnetic phase increases rapidly with increasing pressure. The present XRD observations of the congruent melting of FeH, along with different crystal structures between Fe and FeH, indicate that the Fe-FeH becomes a eutectic system above ~40 GPa (Figure 1c). The recent experiments by Tagawa et al. (2022) demonstrated that fcc FeH is stable at least to 142 GPa and 3660 K. The stability of fcc FeH over the hcp and dhcp structures has been shown by theory (Isaev et al., 2007). It is therefore likely that hcp Fe and fcc FeH form a binary eutectic system also at inner core conditions.

The melting curve of FeH is extrapolated to inner core pressures by our thermodynamic model (Figure 5a). It shows that the melting point of stoichiometric FeH is 5500 K at 330 GPa of the inner core boundary (ICB) pressure. Fe forms a binary eutectic system also with FeSi, FeO, Fe_2S (Tateno et al., 2019), and Fe_7C_3 (Lord et al., 2009; Mashino et al., 2019) at the ICB pressure. The melting curve of FeH is compared to those of these Fe alloys/compounds; FeSi (Lord et al., 2010), FeO (Fischer et al., 2010), FeS (Boehler, 1992) (instead of Fe_2S), and Fe_3C (liquidus curve, Liu et al., 2016) (instead of Fe_7C_3). Note that the dT/dP slope of the melting curve of non-magnetic FeH is larger than those of other endmembers except Fe_3C. On the other hand, it is similar to that of pure Fe, which was obtained also by the present thermodynamic modeling (Figure 5b). FeH melts at only ~350 K below Fe at both the core-mantle boundary (CMB) and the ICB.

The possible eutectic liquid composition in the Fe-FeH system has been estimated to be

$FeH_{0.42}$ (Fe + 0.75 wt% H) at ~40 GPa, based on the liquidus phase relations in Fe-O-H along with the subsolidus phase equilibria of an Fe-H alloy (Oka et al., 2022). The binary eutectic composition is controlled in a large part by the melting points of Fe and FeH endmembers. The similar dT/dP slopes between their melting curves (Figure 5b) suggest that the depression of Fe-FeH eutectic temperature compared to the melting points of Fe and FeH endmembers is little dependent on pressure. The eutectic liquid composition of $FeH_{0.42}$ estimated at ~40 GPa may also change little with increasing pressure. The observed outer core density and velocity can be explained with liquid Fe containing 1.0 wt% H when hydrogen is a single light element in the core (Umemoto & Hirose, 2015, 2020). $FeH_{0.42}$ (Fe + 0.75 wt% H) could be the maximum hydrogen concentration in the liquid core because otherwise FeH would crystallize at the ICB and not form a solid inner core that is denser than the liquid outer core (Tagawa et al., 2022).

5. Conclusions

We carried out high P-T experiments using a laser-heated DAC and determined the melting curve of non-magnetic stoichiometric FeH in a pressure range from 43 and 152 GPa. Melting was recognized on the basis of the appearance of additional hazy signals in 2D XRD images upon quenching temperature, which we confirmed is consistent with the observation of a melting texture on the cross section of a recovered sample. The results demonstrate that the dT/dP slope of the melting curve of non-magnetic FeH is substantially larger than that of the magnetic phase which was determined previously below 20 GPa. Our experiments also show that FeH melts congruently at a temperature maximum in the Fe-H_2 system in the pressure range explored.

These results indicate that the loss of local spin moment in FeH expands its stability with respect to liquid. They also suggest that Fe and non-magnetic FeH form a eutectic system above ~40 GPa, which is supported by the fact that these two adopt different crystal structures, hcp and fcc, respectively. The dT/dP slope of the melting curve of non-magnetic FeH is similar to that of Fe, suggesting that the Fe-FeH eutectic liquid composition, which was estimated to be $FeH_{0.42}$ (Fe + 0.75 wt% H) at ~40 GPa (Oka et al., 2022), will only change to a minor extent with increasing pressure. It gives the upper bound for hydrogen concentration in the outer core, while the observed density and velocity allow the presence of up to 1.0 wt% H in the liquid core (Umemoto & Hirose, 2015, 2020).

Data Availability Statement

Data for this research are found in Tables 1 and 2 available online (from https://doi.org/10.5281/zenodo.6342458).

Acknowledgments

Synchrotron XRD measurements were made at BL10XU, SPring-8 (proposals no. 2018B0072, 2019A0072, 2019B0072, and 2020A0072). This work was supported by the JSPS grants to K.H.

References

Antonov, V. E., Gurev, V. M., Kulakov, V. I., Kuzovnikov, M. A., Sholin, I. A., & Zuykova, V. Y. (2019). Solubility of deuterium and hydrogen in fcc iron at high pressures and temperatures. *Physical Review Materials*, *3*, 113604. https://doi.org/10.1103/PhysRevMaterials.3.113604

Anzellini, S., Dewaele, A., Mezouar, M., Loubeyre, P., & Morard, G. (2013). Melting of iron at Earth's inner core boundary based on fast X-ray diffraction. *Science*, *340*, 464–466. https://doi.org/10.1126/science.1233514

Boehler, R. (1992). Melting of the Fe-FeO and the Fe-FeS systems at high pressure: Constraints on core temperatures. *Earth and Planetary Science Letters*, *111*, 217–227. https://doi.org/10.1016/0012-821X(92)90180-4

Campbell, A. J., Danielson, L., Righter, K., Seagle, C. T., Wang, Y., & Prakapenka, V. B. (2009). High pressure effects on the iron-iron oxide and nickel-nickel oxide oxygen fugacity buffers. *Earth and Planetary Science Letters*, *286*, 556–564. https://doi.org/10.1016/j.epsl.2009.07.022

Chi, Z., Nguyen, H., Matsuoka, T., Kagayama, T., Hirao, N., Ohishi, Y., & Shimizu, K. (2011). Cryogenic implementation of charging diamond anvil cells with H_2 and D_2. *The Review of Scientific Instruments*, *82*, 105109. https://doi.org/10.1063/1.3652981

Dinsdale, A. T. (1991). SGTE data for pure elements. *Calphad*, *15*, 317–425. https://doi.org/10.1016/0364-5916(91)90030-N

Dorogokupets, P. I., & Dewaele, A. (2007). Equations of state of MgO, Au, Pt, NaCl-B1, and NaCl-B2: Internally consistent high-temperature pressure scales. *High Pressure Research*, *27*, 431–446. https://doi.org/10.1080/08957950701659700

Fischer, R., & Campbell, A. J. (2010). High-pressure melting of wüstite. *American Mineralogist*, *95*, 1473–1477. https://doi.org/10.2138/am.2010.3463

Fukai, Y. (1992). Some properties of the Fe-H system at high pressures and temperatures, and their implications for the Earth's core. In Y. Syono, M.H. Manghnani (Eds.), *High-*

371 *pressure research: Applications to Earth and planetary sciences* (Vol. 67, pp. 373–
372 385). https://doi.org/10.1029/GM067p0373
373 Fukai, Y., & Suzuki, T. (1986). Iron–water reaction under high pressure and its
374 implication in the evolution of the Earth. *Journal of Geophysical Research*, *91*, 9222–
375 9230. https://doi.org/10.1029/JB091iB09p09222
376 He, Y., Sun, S., Kim, D.-Y., Jang, B.-G., Li, H., & Mao, H.-K. (2022). Superionic iron
377 alloys and their seismic velocities in Earth's inner core. *Nature*, *602*, 258–262.
378 https://doi.org/10.1038/s41586-021-04361-x
379 Helffrich, G., & Connolly, J. A. D. (2009). Physical contradictions and remedies using
380 simple polythermal equations of state. *American Mineralogist*, *94*, 1616–1619.
381 https://doi.org/10.2138/am.2009.3262
382 Hillert, M., & Jarl, M. (1978). A model for alloying effects in ferromagnetic metals.
383 *Calphad*, *2*, 227–238. https://doi.org/10.1016/0364-5916(78)90011-1
384 Hirao, N., Kondo, T., Ohtani, E., Takemura, K., & Kikegawa, T. (2004). Compression of
385 iron hydride to 80 GPa and hydrogen in the Earth's inner core. *Geophysical Research*
386 *Letters*, *31*, L06616. https://doi.org/10.1029/2003GL019380
387 Hirao, N., Kawaguchi, S. I., Hirose, K., Shimizu, K., Ohtani, E., & Ohishi, Y. (2020).
388 New developments in high-pressure X-ray diffraction beamline for diamond anvil cell
389 at SPring-8. *Matter and Radiation at Extremes*, *5*, 1–10.
390 https://doi.org/10.1063/1.5126038
391 Hirose, K., Tagawa, S., Kuwayama, Y., Sinmyo, R., Morard, G., Ohishi, Y., & Genda, H.
392 (2019). Hydrogen limits carbon in liquid iron. *Geophysical Research Letters*, *46*,
393 5190–5197. https://doi.org/10.1029/2019GL082591
394 Hirose, K., Wood, B., & Vočadlo, L. (2021). Light elements in the Earth's core. *Nature*
395 *Reviews Earth & Environment*, *2*, 645–658. https://doi.org/10.1038/s43017-021-
396 00203-6
397 Ikuta, D., Ohtani, E., Sano-Furukawa, A., Shibazaki, Y., Terasaki, H., Yuan, L., & Hattori,
398 T. (2019). Interstitial hydrogen atoms in face-centered cubic iron in the Earth's core.
399 *Scientific Reports*, *9*, 7108. https://doi.org/10.1038/s41598-019-43601-z
400 Isaev, E. I., Skorodumova, N. V, Ahuja, R., Vekilov, Y. K., & Johansson, B. (2007).
401 Dynamical stability of Fe-H in the Earth's mantle and core regions. *Proceedings of the*
402 *National Academy of Sciences of the United States of America*, *104*, 9168–9171.
403 https://doi.org/10.1073/pnas.0609701104
404 Kato, C., Umemoto, K., Ohta, K., Tagawa, S., Hirose, K., & Ohishi, Y. (2020). Stability
405 of fcc phase FeH to 137 GPa. *American Mineralogist*, *105*, 917–921.
406 https://doi.org/10.2138/am-2020-7153
407 Kivilahti, J. K., & Miettinen, J. M. (1987). A thermodynamic analysis of the Ti-H system.

Calphad, 11, 187–188.
Komabayashi, T. (2014). Thermodynamics of melting relations in the system Fe-FeO at high pressure: Implications for oxygen in the Earth's core. *Journal of Geophysical Research, 119*, 4164–4177. https://doi.org/10.1002/2014JB010980.
Komabayashi, T., & Fei, Y. (2010). Internally consistent thermodynamic database for iron to the Earth's core conditions. *Journal of Geophysical Research*, *115*, doi:10.1029/2009JB006442.
Komabayashi, T., Fei, Y., Meng, Y., & Prakapenka, V. (2009). In-situ X-ray diffraction measurements of the γ-ε transition boundary of iron in an internally-heated diamond anvil cell. *Earth and Planetary Science Letters*, *282*, 252–257. https://doi.org/10.1016/j.epsl.2009.03.025
Li, Y., Vočadlo, L., Sun, T., & Brodholt, J. P. (2020). The Earth's core as a reservoir of water. *Nature Geoscience*, *13*, 453–458. https://doi.org/10.1038/s41561-020-0578-1
Liu, J., Lin, J., Prakapenka, V.B., Prescher, C., & Yoshino, T. (2016). Phase relations of Fe_3C and Fe_7C_3 up to 185 GPa and 5200 K: Implication for the stability of iron carbide in the Earth's core. *Geophysical Research Letters*, *43*, 12415–12422. https://doi.org/ 10.1002/2016GL071353.
Lord, O. T., Walter, M. J., Dasgupta, R., Walker, D., & Clark, S. M. (2009). Melting in the Fe–C system to 70 GPa. *Earth and Planetary Science Letters*, *284*, 157–167. https://doi.org/10. 1016/j.epsl.2009.04.017.
Lord, O. T., Walter, M. J., Dobson, D. P., Armstrong, L., Clark, S. M., & Kleppe, A. (2010). The FeSi phase diagram to 150 GPa. *Journal of Geophysical Research*, *115*, B06208. doi:10.1029/2009JB006528.
Mashino, I., Miozzi, F., Hirose, K., Morard, G., & Sinmyo, R. (2019). Melting experiments on the Fe-C binary system up to 255 GPa: Constraints on the carbon content in the Earth's core. *Earth and Planetary Science Letters*, *515*, 135–144. https://doi.org/10.1016/j.epsl.2019.03.020
Mori, Y., Ozawa, H., Hirose, K., Sinmyo, R., Tateno, S., Morard, G., & Ohishi, Y. (2017). Melting experiments on Fe–Fe_3S system to 254 GPa. *Earth and Planetary Science Letters*, *464*, 135–141. https://doi.org/10.1016/j.epsl.2017.02.021
Ohta, K., Ichimaru, K., Einaga, M., Kawaguchi, S., Shimizu, K., Matsuoka, T., et al. (2015). Phase boundary of hot dense fluid hydrogen. *Scientific Reports*, *5*, 16560. https://doi.org/10.1038/srep16560
Oka, K., Tagawa, S., Hirose, K., & Ohishi, Y. (2022). Melting experiments on Fe-O-H: Evidence for eutectic melting in Fe-FeH and implications for hydrogen in the core. *Earth and Space Science Open Archive*. https://doi.org/10.1002/essoar.10510359.1
Pépin, C. M., Dewaele, A., Geneste, G., Loubeyre, P., & Mezouar, M. (2014). New iron

hydrides under high pressure. *Physical Review Letters*, *113*, 265504. https://doi.org/10.1103/PhysRevLett.113.265504

Piet, H., Chizmeshya, A. V. G., Chen, B., Chariton, S., Greenberg, E., Prakapenka, V. B., & Shim, S.-H. (2021). Effect of nickel on the high-pressure phases in FeH. *Physical Review B*, *104*, 224106. https://doi.org/10.1103/PhysRevB.104.224106

Raymond, S. N., Quinn, T., & Lunine, J. I. (2007). High-resolution simulations of the final assembly of Earth-like planets. 2. Water delivery and planetary habitability. *Astrobiology*, *7*, 66–84. https://doi.org/10.1089/ast.2006.06-0126.

R Core Team (2018). *R: A language and environment for statistical computing*. R Foundation for Statistical Computing. Vienna, Austria.

Sakamaki, K., Takahashi, E., Nakajima, Y., Nishihara, Y., Funakoshi, K., Suzuki, T., & Fukai, Y. (2009). Melting phase relation of FeH_x up to 20 GPa: Implication for the temperature of the Earth's core. *Physics of the Earth and Planetary Interiors*, *174*, 192–201. https://doi.org/10.1016/j.pepi.2008.05.017

Sato, T., Okuzumi, S., & Ida, S. (2016). On the water delivery to terrestrial embryos by ice pebble accretion. *Astronomy & Astrophysics*, *589*, A15. https://doi.org/10.1051/0004-6361/201527069

Shibazaki, Y., Terasaki, H., Ohtani, E., Tateyama, R., Nishida, K., Funakoshi, K., & Higo, Y. (2014). High-pressure and high-temperature phase diagram for $Fe_{0.9}Ni_{0.1}$-H alloy. *Physics of the Earth and Planetary Interiors*, *228*, 192–201. https://doi.org/10.1016/j.pepi.2013.12.013

Stähler, S. C., Khan, A., Banerdt, W. B., Lognonné, P., Giardini, D., Ceylan, S., et al. (2021). Seismic detection of the martian core. *Science*, *373*, 443–448. https://doi.org/10.1126/science.abi7730

Sugimoto, H., & Fukai, Y. (1992). Solubility of hydrogen in metals under high hydrogen pressures: thermodynamical calculations. *Acta Metallurgica et Materialia*, *40*, 2327–2336. https://doi.org/10.1016/0956-7151(92)90151-4

Tagawa, S., Ohta, K., Hirose, K., Kato, C., & Ohishi, Y. (2016). Compression of Fe-Si-H alloys to core pressures. *Geophysical Research Letters*, *43*, 3686–3692. https://doi.org/10.1002/2016GL068848

Tagawa, S., Sakamoto, N., Hirose, K., Yokoo, S., Hernlund, J., Ohishi, Y., & Yurimoto, H. (2021). Experimental evidence for hydrogen incorporation into Earth's core. *Nature Communications*, *12*, 2588. https://doi.org/10.1038/s41467-021-22035-0

Tagawa, S., Gomi, H., Hirose, K., & Ohishi, Y. (2022). High-temperature equation of state of FeH: Implications for hydrogen in Earth's inner core. *Geophysical Research Letters*, *49*, e2021GL096260. https://doi. org/10.1029/2021GL096260

Tateno, S., Ozawa, H., Hirose, K., Suzuki, T., I-Kawaguchi, S., & Hirao, N. (2019). Fe_2S:

The most Fe-rich iron sulfide at the Earth's inner core pressures. *Geophysical Research Letters*, *46*, 11944–11949. https://doi.org/ 10.1029/2019GL085248

Thompson, E. C., Davis, A. H., Bi, W., Zhao, J., Alp, E. E., Zhang, D., et al. (2018). High-pressure geophysical properties of fcc phase FeH_x. *Geochemistry, Geophysics, Geosystems*, *19*, 305–314. https://doi.org/10.1002/2017GC007168

Umemoto, K., & Hirose, K. (2015). Liquid iron-hydrogen alloys at outer core conditions by first-principles calculations. *Geophysical Research Letters*, *42*, 7513–7520. https://doi.org/10.1002/2015GL065899

Umemoto, K., & Hirose, K. (2020). Chemical compositions of the outer core examined by first principles calculations. *Earth and Planetary Science Letters*, *531*, 116009. https://doi.org/10.1016/j.epsl.2019.116009

Walsh, K. J., Morbidelli, A., Raymond, S. N., O'brien, D. P., & Mandell, A. M. (2011). A low mass for Mars from Jupiter's early gas-driven migration. *Nature*, *475*, 206–209. https://doi.org/10.1038/nature10201

Wang, W., Li, Y., Brodholt, J. P., Vočadlo, L., Walter, M. J., & Wu, Z. (2021). Strong shear softening induced by superionic hydrogen in Earth's inner core. *Earth and Planetary Science Letters*, *568*, 117014. https://doi.org/10.1016/j.epsl.2021.117014

Yoshizaki, T., & McDonough, W. F. (2020). The composition of Mars. *Geochimica et Cosmochimica Acta*, *273*, 137–162. https://doi.org/10.1016/j.gca.2020.01.011

Yuan, L., & Steinle-Neumann, G. (2020). Strong sequestration of hydrogen into the Earth's core during planetary differentiation. *Geophysical Research Letters*, *47*, e2020GL088303. https://doi.org/10.1029/2020GL088303

Zinkevich, M., Mattern, M., Handstein, A., & Gutfleisch, O. (2002). Thermodynamics of Fe-Sm, Fe-H, and H-Sm systems and its application to the hydrogen-disproportionation-desorption-recombination (HDDR) process for the system $Fe_{17}Sm_2$-H_2. *Journal of Alloys and Compounds*, *339*, 118–139. https://doi.org/10.1016/S0925-8388(01)01990-9

510

Table 1

Experimental Results

Run #	Pressure (GPa)	Temperature (K)	
		T_{max}	T_{mean}
Melting			
1	69 (7)	2740 (120)	2520 (110)
2	152 (15)	4630 (220)	4490 (210)
3	121 (12)	3860 (180)	3630 (170)
	142 (14)	4210 (200)	3970 (180)
4	45 (4)	2110 (90)	2060 (90)
5	47 (5)	2170 (90)	2100 (90)
Not-melting			
1	67 (7)	2480 (110)	2340 (100)
2	149 (15)	3900 (180)	3550 (160)
3	113 (11)	3560 (160)	3410 (160)
	135 (13)	3610 (170)	3500 (160)
4	43 (4)	1830 (80)	1750 (70)

511

512

Table 2

Physical properties

Property	Value	Scale and Units	Source (if not this study)
V_0 volume			
(Fe bcc)	0.71000	J bar^{-1}	
(Fe fcc)	0.68640	J bar^{-1}	
(Fe hcp)	0.67357	J bar^{-1}	
(Fe liq)	0.70205	J bar^{-1}	
(H fcc)	0.12861	J bar^{-1}(mol. at. H)$^{-1}$	A
(H liq)	0.06437	J bar^{-1}(mol. at. H)$^{-1}$	
α thermal expansivity			
b_1 (Fe bcc)	3.05500	10^{-6} K^{-1}	
b_3 (Fe bcc)	-9.80000	10^{-3}	
b_1 (Fe fcc)	9.4310	10^{-6} K^{-1}	
b_1 (Fe hcp)	1.1630	10^{-5} K^{-1}	
b_1 (Fe liq)	2.7720	10^{-5} K^{-1}	
b_1 (H fcc)	7.989	$\times 10^{-6}$ K^{-1} (mol. at. H)$^{-1}$	A
b_2 (H fcc)	2.093	$\times 10^{-8}$ K^{-2} (mol. at. H)$^{-1}$	A
b_1 (H liq)	7.385	$\times 10^{-5}$ K^{-1} (mol. at. H)$^{-1}$	
K bulk modulus			
(Fe bcc)	164	GPa	D
(Fe fcc)	165.3	GPa	D
(Fe hcp)	165	GPa	D
(Fe liq)	148	GPa	
(H fcc)	-2.75	GPa (mol. at. H)$^{-1}$	A
(H liq)	110.86	GPa (mol. at. H)$^{-1}$	
K' bulk modulus pressure derivative			
(Fe bcc)	5.29		D
(Fe fcc)	5.5		D
(Fe hcp)	4.97		D
(Fe liq)	6.39		
(H fcc)	-0.99	(mol. at. H)$^{-1}$	A
(H liq)	-1.90	(mol. at. H)$^{-1}$	
T_C Curie temperature			
(Fe bcc)	1043	K	B
(Fe fcc)	67	K	B
(H fcc)	2242	K	
β magnetic moment			
(Fe bcc)	2.22	μ_B	B
(Fe fcc)	0.7	μ_B	B
(H fcc)	1.45	μ_B	
p magnetic enthalpy fraction			
(all fcc)	0.28		C
(all bcc)	0.4		C

Notes. $\alpha_{\mathrm{FeHx}}(T,x) = b_1(x) + b_2(x)T + b_3(x)/T$; $b_i(x) = b_{i,\mathrm{Fe}} + xb_{i,\mathrm{H}}$

$V_{\mathrm{FeHx}}(x) = V_{\mathrm{Fe}} + xV_{\mathrm{H}}$; $K_{\mathrm{FeHx}}(x) = K_{\mathrm{Fe}} + xK_{\mathrm{H}}$; $K'_{\mathrm{FeHx}}(x) = K'_{\mathrm{Fe}} + xK'_{\mathrm{H}}$

$T_{C,x} = T_{C,\mathrm{Fe}} + xT_{C,\mathrm{H}}$; $\beta_x = \beta_{\mathrm{Fe}} + x\beta_{\mathrm{H}}$.

μ_B - Bohr magneton unit.

Sources: A - Tagawa et al. (2022); B - Dinsdale (1991); C - Hillert & Jarl (1978); D - Komabayashi & Fei (2010).

513

514

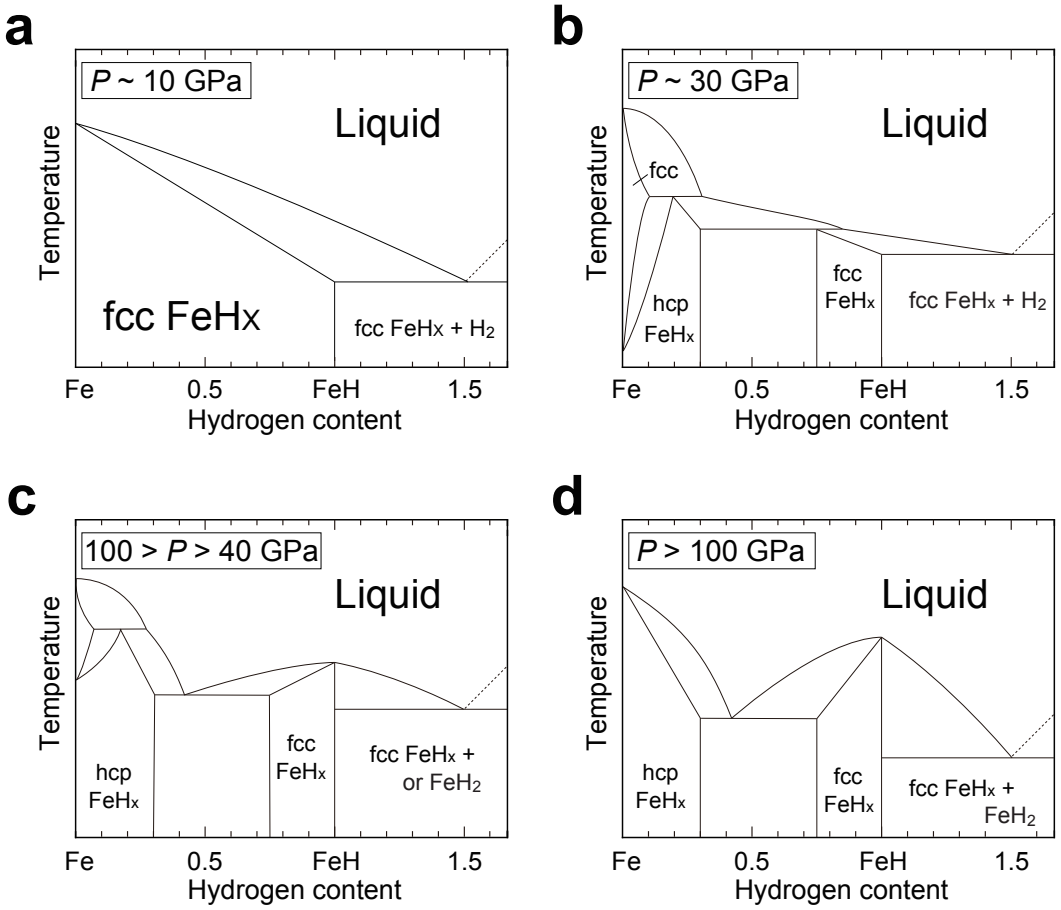

515

516 **Figure 1.** Changes in the Fe-H phase diagram with increasing pressure. (a) Fe and FeH
517 form continuous solid solution at ~10 GPa, where the solidus temperature of magnetic
518 FeH corresponds to the eutectic temperature between FeH and H_2 (Fukai, 1992). (b) The
519 appearance of the hcp phase on the Fe-rich portion leads to the gap in solid solution and
520 the peritectic points between Fe and FeH. (c) FeH loses the local spin moment and melts
521 congruently with a temperature maximum above ~40 GPa. Fe and FeH form eutectic
522 melting with the eutectic liquid composition of $FeH_{0.42}$ (Oka et al., 2022). (d) The
523 formation of FeH_2 (Pépin et al., 2014) results in eutectic melting between FeH and FeH_2.
524 The depression of Fe-FeH eutectic temperature and the eutectic liquid composition likely
525 change little with increasing pressure.
526

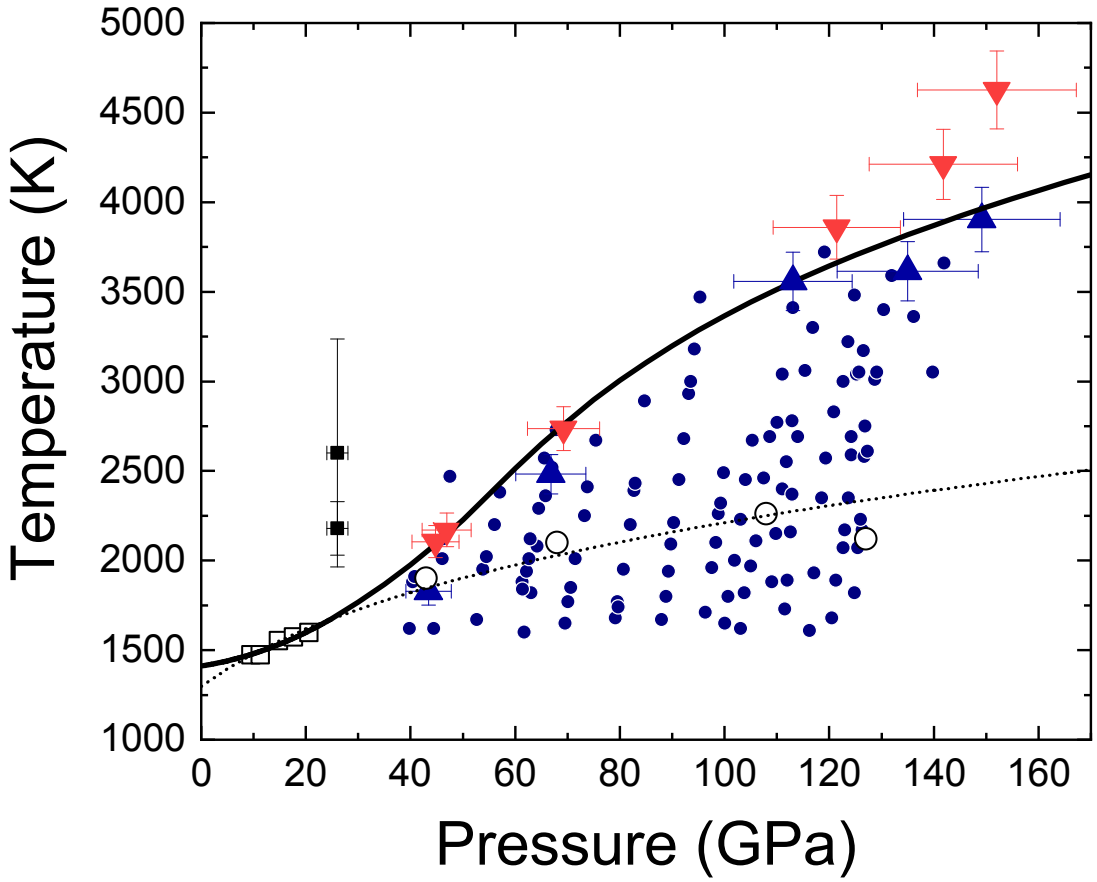

Figure 2. Experimental data and calculated melting curve of stoichiometric FeH. Present experimental conditions of melting (red, inverse triangles) and non-melting (blue, normal triangles) are plotted along with those where the unit-cell volume was determined for solid FeH in a previous study (Tagawa et al., 2022) (small blue circles). Those reported by recent experiments (Piet et al., 2021) are also shown (small squares). Dotted curve represents eutectic melting temperature between FeH and H_2/FeH_2 based on the solidus temperatures of magnetic FeH (open squares) (Sakamaki et al., 2009) and FeH_x ($1 < x < 2$) (open circles) (Hirose et al., 2019). The dT/dP slope of the melting curve of non-magnetic FeH is substantially larger than that of the non-magnetic phase.

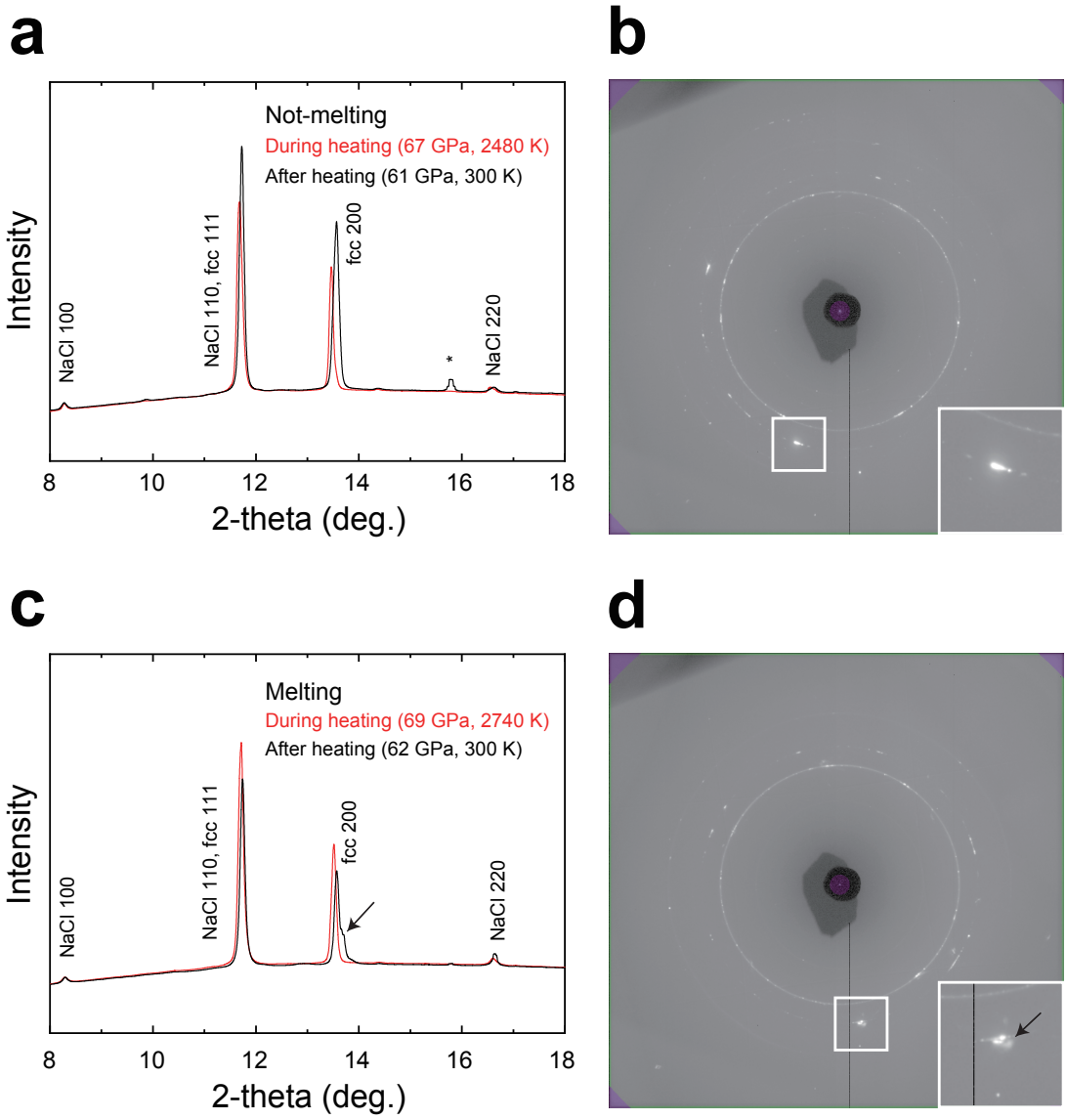

Figure 3. XRD patterns collected in run #1. (a) Melting did not occur when heating FeH to T_{max} = 2480 K; additional XRD peaks were not observed upon quenching temperature to 300 K. (b) Partially molten sample was quenched from T_{max} = 2740 K to room temperature. The hazy diffraction signal appeared close to the fcc peaks because of the formation of incomplete crystals from liquid upon temperature quenching.

549

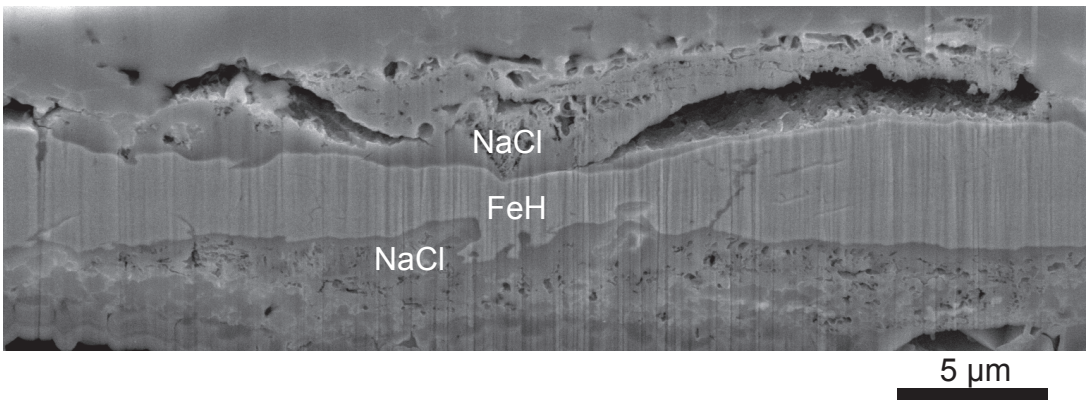

550

551 **Figure 4.** Scanning electron microscope image of the melting texture of FeH observed
552 on the sample cross section recovered from run #1. The presence of NaCl grains (pressure
553 medium) in FeH metal showed that the sample was molten during heating.
554

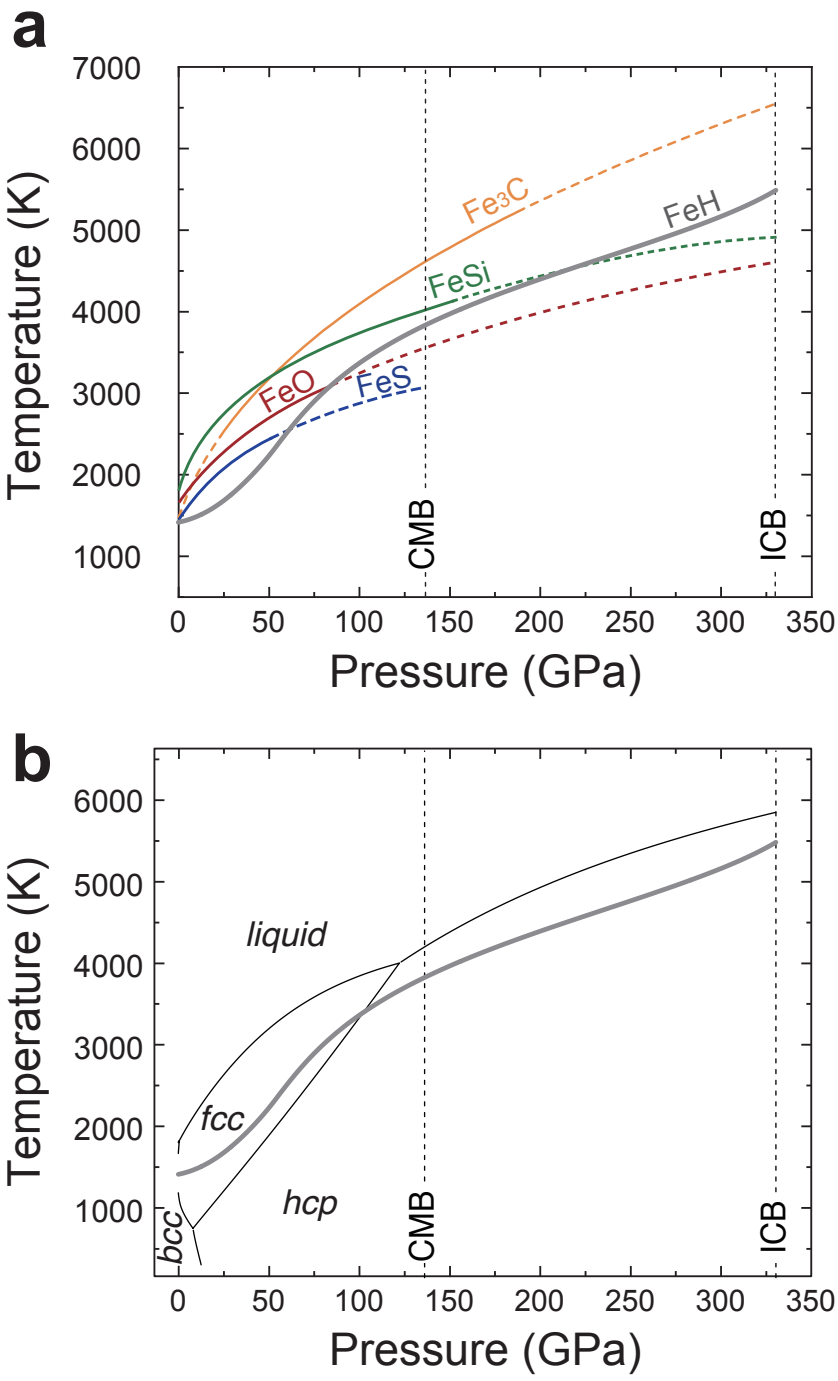

555

556 **Figure 5.** (a) Comparison of the melting curve of FeH (gray) with those of FeSi (green)
557 (Lord et al., 2010), FeO (brown) (Fischer et al., 2010), FeS (blue) (Boehler, 1992), and
558 Fe_3C (yellow, liquidus curve) (Liu et al., 2016). Fe forms eutectic system with these
559 alloys/compounds in each binary system at the ICB pressure of 330 GPa (Fe_2S and Fe_7C_3
560 instead of FeS and Fe_3C, respectively). (b) Calculated phase diagram for Fe (black thin
561 lines) and FeH melting (gray bold line). Iron phase fields are labeled.